Chapter 4

Possible topological Hall effect in the Mn_2CoAl Heusler compound

This work has been published in *Nisha Shahi et al., Phys. Status Solidi - Rapid Res. Lett., 2300352 (2023)*

This chapter contains evidence of a giant THE over a wide temperature range (2-300 K) in the bulk Mn_2CoAl compound, which may arise due to the microscopic non-coplanar magnetic structure, resulting from the interplay between the cubic MCA, the ferro- and antiferromagnetic exchange interactions.

4.1 Introduction

Topological Hall effect (THE) is one of the exotic transport phenomena that serves as a powerful tool [1, 2, 3, 4, 5, 6] for detecting non-coplanar magnetic textures, which have potential applications as memory and logic elements of future spintronic based devices [7, 8, 9, 10]. Magnetic materials with the non-coplanar spin texture often exhibit the THE as an additional Hall contribution along with the ordinary and anomalous Hall [1, 11, 12]. The ordinary Hall effect arises due to the Lorentz force experienced by the charge carriers in a current-carrying conductor placed in the perpendicular magnetic field [13, 14]. In ferro-/ferrimagnetic conductors, an anomalous Hall contribution has been found as a combined effect of spin orbit coupling and magnetization [14, 15, 16, 17, 18]. The strength of the ordinary and anomalous Hall effect has been observed to be proportional to the applied magnetic field and the magnetization of material, respectively [14]. Furthermore, in the presence of a non-coplanar magnetic texture, the charge carriers experience a fictitious magnetic field. This fictitious field introduces a real space Berry phase in the wave function of the charge carriers, giving rise to an extra Hall contribution, which scales neither the magnetic field nor the magnetization [11, 19]. This emergent Hall contribution is typically observed due to the topologically stable non-coplanar spin textures such as skyrmion and is therefore named as the THE [1, 12].

The THE caused by the real space Berry curvature associated with the skyrmion like mesoscopic topological spin textures have been observed in various magnetic materials, including B20 compounds [20, 21, 22], perovskites [19, 23], and Heusler compounds [24, 25]. Besides skyrmion, the THE has also been observed due to the real space Berry curvature accompanied with microscopic non-coplanar spin texture with non-vanishing spin chirality [$S_i.(S_j \times S_k) \neq 0$, where S_i, S_j and S_k are three neighboring spins making a particular solid angle] [4, 6], which is recently termed as the spin chirality Hall effect [26]. However, to be consistent with previous literature, we will proceed us-

ing THE. The non-coplanar spin texture induced large THE, has been realized in the geometrically frustrated antiferromagnets such as Mn_5Si_3 [4], Mn_3Ga[27], and $Fe_{1.3}Sb$[28] with centrosymmetric hexagonal crystal structure. In these magnets, the evolution of non-coplanar magnetic structure occurs due to out of plane spin canting as a result of the interplay between uniaxial magneto-crystalline anisotropy (MCA) and weak structural distortion/defect [4, 27, 28]. In addition, Fe doped Mn_3Sn [29, 30] and Mn_3Ge [31], and YMn_6Sn_6 [32] hexagonal compounds have recently been observed to exhibit a large THE due to the non-coplanar spin structure, stabilized as a result of the competition between Heisenberg exchange interactions and uniaxial MCA.

In recent past, the investigation of THE [33, 35, 36] in Heusler compounds has gained vast interest due to tunability of their electronic and magnetic properties [37, 38]. The THE in the noncentrosymmetric tetragonal Heusler compounds such as Mn_2NiGa [33], $Mn_{1.4}Pt_{0.9}Pd_{0.1}Sn$ [34, 35], and $Mn_{1.4}PtSn$ [39] has been found due to topologically stable antiskyrmionic phase, developed by the interplay between Dzyaloshinskii-Moriya interaction (DMI), Heisenberg exchange interaction, and uniaxial MCA. The THE in the centrosymmetric hexagonal Heusler compounds like NiMnGa [36], and MnPdGa [40], has been observed due to the emergence of biskyrmionic topological phase resulting from the competition between the uniaxial MCA and magnetic dipole-dipole interaction. Besides skyrmionic phases, a robust THE in $Mn_{2-x}PtIn$ tetragonal Heusler compound with D_{2d} symmetry has recently been observed due to the microscopic non-coplanar spin texture with non-zero spin chirality as a result of the interplay between DMI, Heisenberg exchange interactions, and uniaxial MCA [41]. Not only the tetragonal and hexagonal but the cubic Heusler compound like NiMnIn has also been found to exhibit THE due to the skyrmion like non-coplanar spin texture arising from the presence of cubic MCA [42]. However, the cubic Heusler compounds have rarely been investigated in this context due to the unanticipated bulk DMI and uniaxial MCA.

In spintronics, one of the critical challenges is to find suitable materials that can retain their magnetic properties at room temperature or higher temperature [43]. In this context, the high Curie temperature Mn_2CoAl cubic Heusler compound, which exhibits spin gapless semiconducting behaviour [44] consisting of a finite gap in one spin channel and a close gap in another, has gained tremendous interest [45, 46]. Recently, skyrmionic topological Hall effect has been observed in the thin film form of the Mn_2CoAl compound due to interfacial DMI in the system [47]. Although the Mn_2CoAl

compound is non-centrosymmetric (space group $F\bar{4}3m$) but the space group do not support bulk DMI (similar to the centrosymmetric magnets) as per the reported analysis on the point group dependency of micromagnetic DMI [48]. Interestingly, the literature suggests a strong magnetic frustration due to the presence of both ferro- and antiferromagnetic type Heisenberg exchange interaction along with the disorder in the Mn_2CoAl compound [49, 50, 51]. Therefore, the competition between the cubic MCA, which is expected in the cubic crystal systems [42], and the Heisenberg exchange interactions may create the non-coplanar spin texture [29, 30, 32, 42]. This motivated us to search for the possible THE in the bulk Mn_2CoAl compound.

In this chapter, we present the observation of a large THE over a wide temperature range by performing the magnetic and transport measurements in a bulk Mn_2CoAl cubic Heusler compound. The AC susceptibility with the magnetic field shows a smooth and continuous behaviour rather than any anomaly, suggests that the observed THE may be related to the microscopic non-coplanar spin textures. The detailed experimental and theoretical investigations suggest that the interplay between ferro- and antiferromagnetic exchange interactions, and the cubic MCA gives rise to the non-coplanar spin texture, which results in the THE in the bulk Mn_2CoAl. This finding may open up further research opportunity in exploring emergent phenomena in the cubic Heusler compounds.

4.2 Results and discussion

4.2.1 Topological Hall Analysis

The details of the sample preparation and characterization methods of the Mn_2CoAl compound are reported elsewhere [52]. The temperature dependent magnetization curve of field cooled warming (FCW) protocol in the temperature range of 2-400 K at a magnetic field of 0.1 T [Fig. 4.1] exhibits a dip type anomaly around 150 K. The dip may be attributed to some antiferromagnetic component because of the strong magnetic frustration, which is anticipated due to the coexistence of ferro- and antiferro-magnetic exchange interaction between the magnetic spins [49, 50, 51]. Such dip or hump kind of anomaly in M-T data has been observed in various compounds because of the coexistence of ferro- and anti-ferromagnetic exchange interaction [30, 31, 53, 54]. Around the same temperature, literature suggests the change in resistivity as well as Seebeck effect [44, 52, 93].

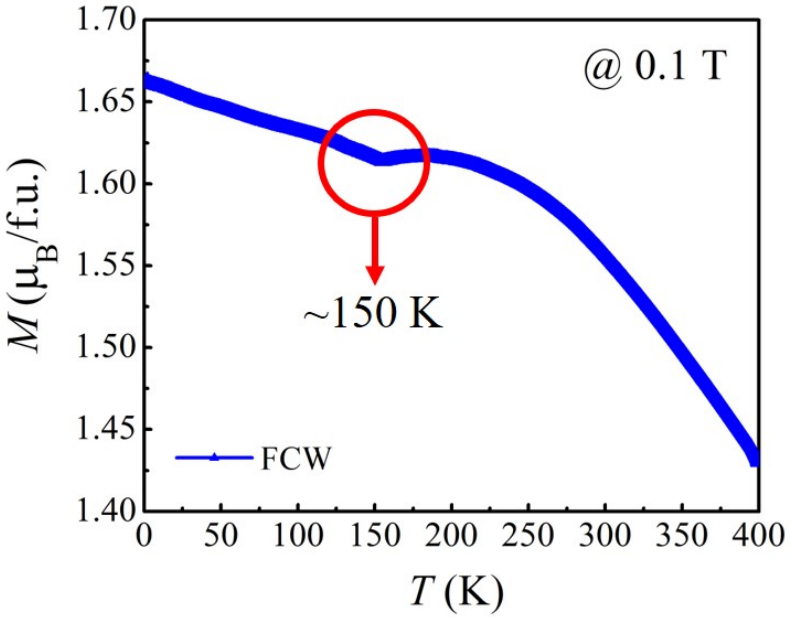

Figure 4.1: Temperature dependent magnetization (M) curve of the Mn_2CoAl compound at 0.1 T magnetic field.

Magnetization isotherms (*M(H)*) and Hall resistivity (ρ_{xy}) data at different temperatures (in the range of 2-300 K) up to a magnetic field of $\pm$1.5 T are shown in Fig. 4.2(a) and (b), respectively. The *M(H)* at 2 K and 300 K, and the ρ_{xy} data are taken from our recent study on the Mn_2CoAl compound [52]. Interestingly, the ρ_{xy} does not follow the *M(H)* data in the low magnetic field region as shown in Fig. 4.2(c) and (d) at 2 K and 300 K, respectively [11, 56]. This divergence is possibly due to the presence of THE in the bulk Mn_2CoAl compound [56].

The ρ_{xy} is generally consist of three contributions, i.e., the ordinary Hall resistivity (ρ_O) proportional to the magnetic field (H) ($\rho_O = R_O H$, where R_O is the ordinary Hall coefficient), the anomalous Hall resistivity (ρ_{AH}) proportional to the magnetization (M), and the topological Hall resistivity (ρ_T) due to the real space Berry curvature associated with non-coplanar spin texture [14, 57, 58]. The ρ_{AH} in a magnetic material may arise from the both intrinsic and extrinsic mechanisms [14, 57]. The intrinsic mechanism is related to the momentum space Berry curvature associated with the electronic band structure, whereas the extrinsic mechanism receives contribution from skew scattering and side jump mechanisms [14, 57]. Our previous study on the Mn_2CoAl compound suggests that the ρ_{AH} is mainly originated by the intrinsic mechanism ($\rho_{AH} = R_S {\rho_{xx}}^2 M$, where ρ_{xx}

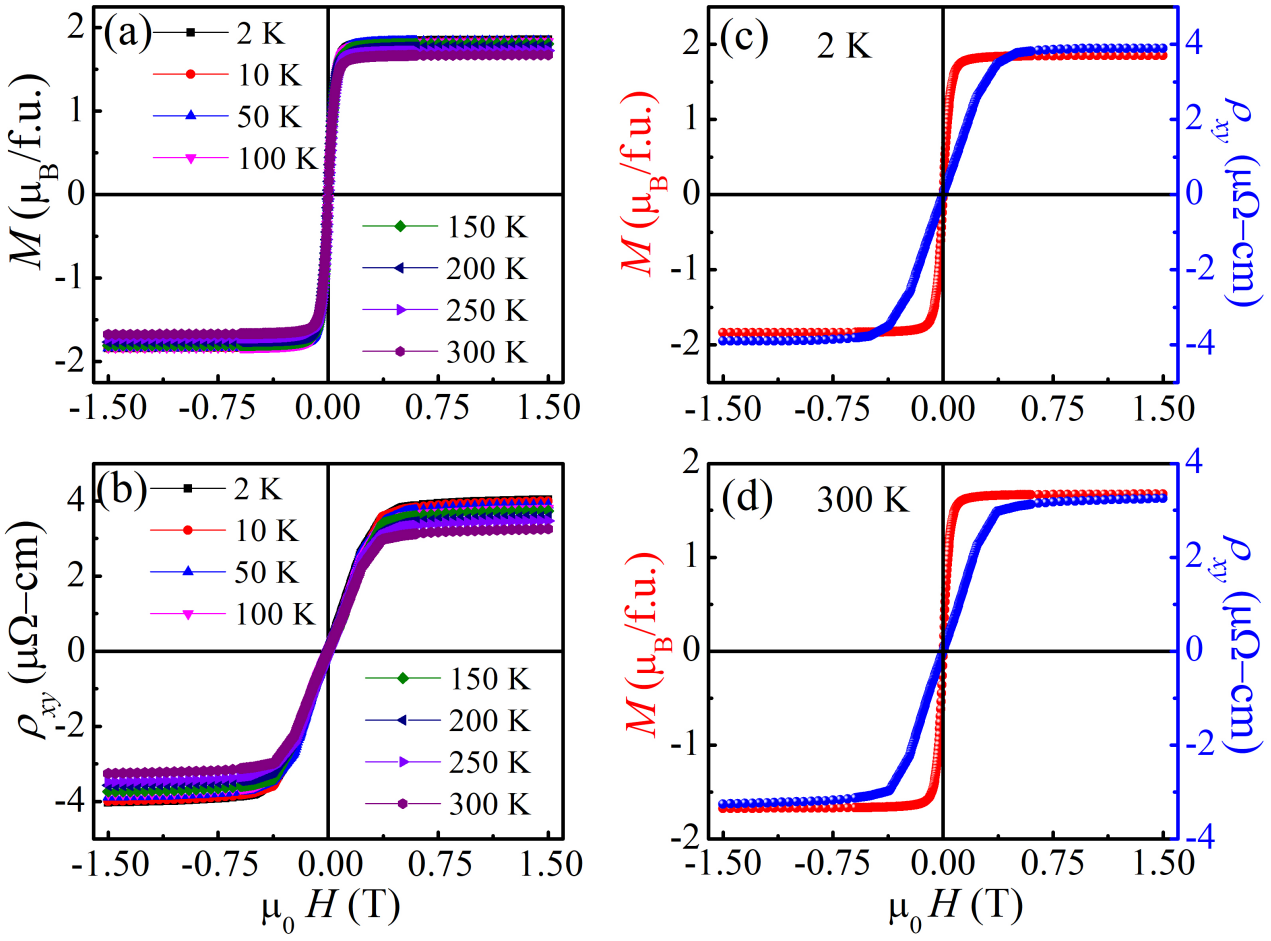

Figure 4.2: figure
(a) The isothermal field-dependent magnetization at different temperatures. (b) Field-dependent Hall resistivity curves at different temperatures [52]. (c) and (d) Combined plot of anomalous Hall resistivity, and field-dependent magnetization for the Mn_2CoAl system at 2 K and 300 K, respectively.

and R_S are longitudinal resistivity and the anomalous Hall coefficient, respectively) [52]. Therefore, the ρ_{xy} can be expressed as [1, 14]-

$$\rho_{xy} = R_O H + R_S \rho_{xx}^2 M + \rho_T \tag{4.1}$$

Fig. 4.2(c) and (d) indicate that the ρ_{xy} follows the *M(H)* data perfectly above the magnetic field of around 1 T. This observation suggests that when the magnetic field is large enough, the ρ_T is supposed to be zero due to the complete disappearance of the non-coplanar spin textures [59, 60]. Therefore, in the high field region ($>$ 1 T), the above equation can be expressed as [59]-

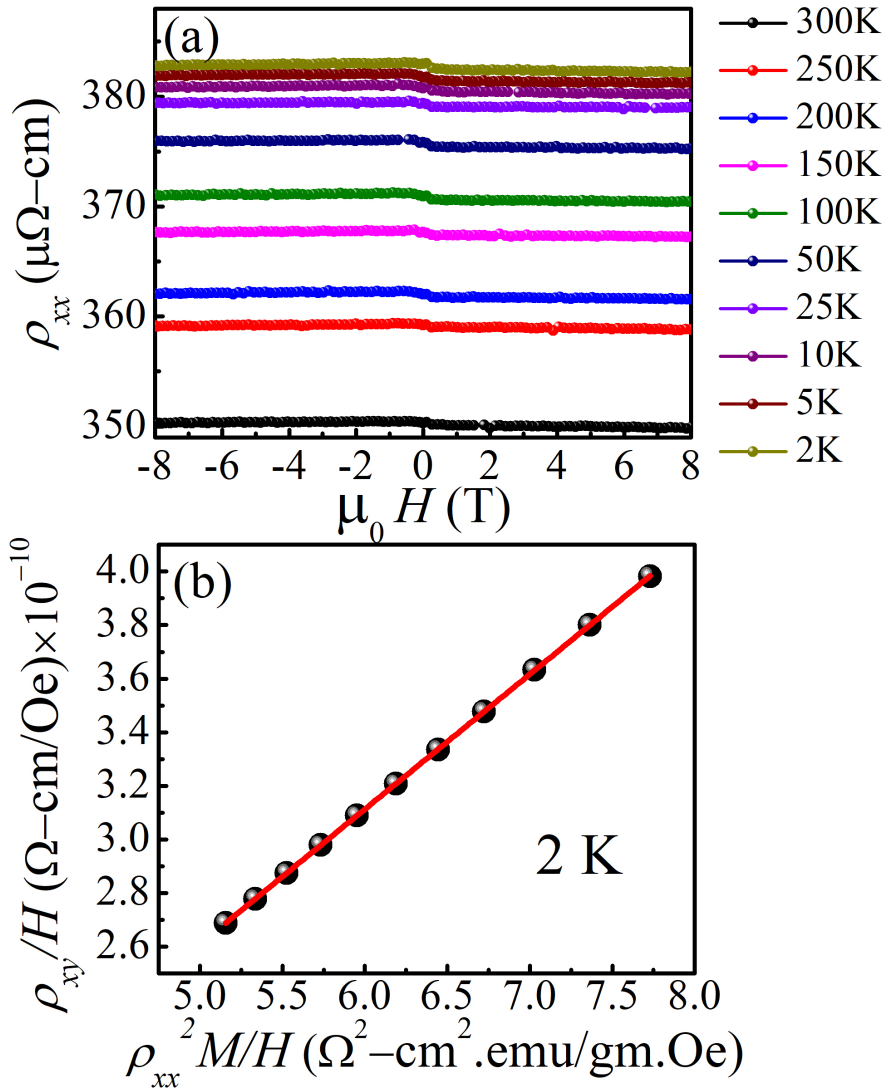

Figure 4.3: (a) Magnetic field dependent longitudinal resistivity (ρ_{xx}-H) data at different temperatures. (b) Linear fitting of $\frac{\rho_{xy}}{H}$ and $\frac{\rho_{xx}^2 M}{H}$ in the high magnetic field region to extract the topological Hall resistivity from the total Hall resistivity (ρ_{xy}).

$$\rho_{xy} = R_O H + R_S \rho_{xx}^2 M \tag{4.2}$$

The expected ρ_T in the low magnetic field region is extracted out from the total ρ_{xy} by carrying out the fitting of the high-field Hall data with Eq. (4.2) using ρ_{xx} versus H [Fig. 4.3 (a)] and *M(H)* data. In this procedure, to calculate the coefficients R_O and R_S, we have first plotted $\frac{\rho_{xy}}{H}$ versus $\frac{\rho_{xx}{}^2 M}{H}$ data (black sphere) in high field region (>1 T) and then performed linear fitting (red line) with the reduced relation (divide the Eq. (4.2) by H), i.e., $\frac{\rho_{xy}}{H} = R_O + \frac{R_S \rho_{xx}{}^2 M}{H}$, as shown in Fig. 4.3 (b). The coefficients R_O and R_S are the intercept and slope of the linear fitting. The Eq. (4.2) will be valid

for low field region (< 1 T) if $\omega_c\tau << 1$, where $\omega_c = \frac{eH}{m}$ is cyclotron frequency and $\tau = \frac{m}{ne^2\rho_{xx}}$ is electron scattering time [4]. Here, e and m are the charge and mass of the electron, and n is the carrier concentration, reported in our previous study [52]. The calculated value of $\omega_c\tau$ is around $0.00034 << 1$ up to 1.5 T field, and the condition $\omega_c\tau << 1$ is followed in the entire temperature range (2-300 K). Therefore, we calculated the ρ_{xy} using the Eq. (4.2) in the whole magnetic field region (0-1.5 T) with the help of the obtained value of the coefficients R_O and R_S. After that, we plotted the calculated ρ_{xy} (black line of Fig. 4.4(a) and (b)) with the experimental ρ_{xy} (blue sphere of Fig. 4.4(a) and (b)). Fig. 4.4(a) and (b) clearly show that the calculated and experimental ρ_{xy} is not overlapping on each other in the low field region, which explicitly indicates the presence of THE. At last, the value of ρ_T [red sphere of Fig. 4.4(a) and (b)] is obtained by subtracting the calculated ρ_{xy} from the experimental ρ_{xy}.

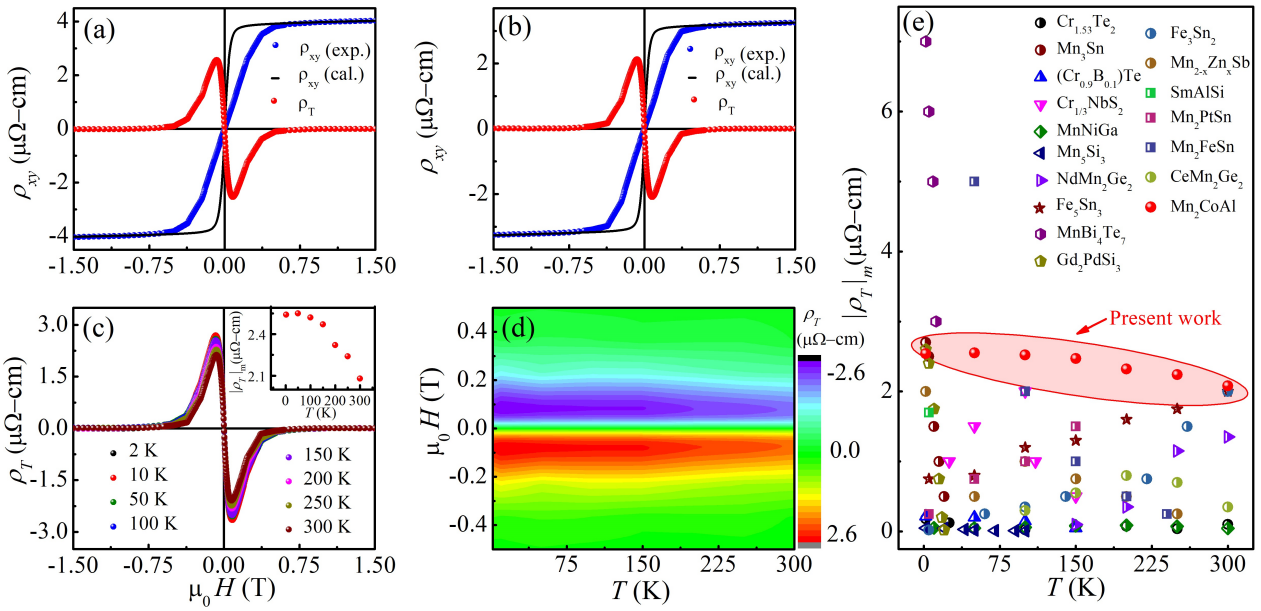

Figure 4.4: (a) and (b) Combined plot of experimental Hall resistivity (blue sphere), calculated Hall resistivity (black line), and topological Hall resistivity (red sphere) at 2 K and 300 K, respectively. (c) Variation of the calculated topological Hall contribution (ρ_T) with the magnetic field at different temperatures. The inset shows variation in the maximum absolute value of topological Hall resistivity ($|\rho_T|_m$) with temperature. (d) Contour plot of THE as a function of temperature and magnetic field. (e) Comparison of the maximum absolute value of topological Hall resistivity ($|\rho_T|_m$) obtained in the present study with previously reported values [4, 12, 19, 30, 36, 59, 60, 61, 62, 63, 64, 65, 66, 67, 68, 69, 70]. We have listed the variation in topological Hall resistivity with respect to temperature.

The ρ_T at different temperatures, as shown in Fig. 4.4(c), is maximum around the magnetic field of 0.1 T and nearly vanishes above the field of ∼0.3 T due to the appearance of spin-polarized state in the high field region. The inset of Fig. 4.4(c) represents the variation in maximum ρ_T with temper-

ature, which indicates that the THE is slightly decreasing with the increase in temperature. The ρ_T reaches to its maximum value of about 2.6 $\mu\Omega$-cm at 2 K, and the minimum value of about 2 $\mu\Omega$-cm at 300 K. To clearly observe the variation in the THE with the magnetic field and temperature (T), we create a contour plot [Fig. 4.4(d)] of the H-T phase diagram. The contour mapping shows that a large ρ_T persists up to room temperature around the field of 0.1 T and it converges to zero above the field of $\sim$0.3 T. Similar behavior has been observed in various systems due to fully spin polarized state at higher magnetic field [4, 27, 28, 29, 30, 31, 32, 33, 34, 35, 39]. The comparison with the previously reported bulk systems [4, 12, 19, 30, 36, 59, 60, 61, 62, 63, 64, 65, 66, 67, 68, 69, 70] [Fig. 4.4(e)] indicates that the large topological Hall persists in the wider temperature range of 2-300 K, which make the Mn_2CoAl compound an ideal platform for the spintronic applications. The moderate decrease in the maximum ρ_T with temperature can be ascribed to the microscopic non-coplanar spin texture [4, 28, 29, 32]. Although, this kind of behaviour in the ρ_T has also been anticipated due to the topological mesoscopic spin texture [12, 36]. Therefore, to explore the underlying cause of the observed THE, we have planned to carry out AC-susceptibility measurement, which is well known for its ability to serve as a probe for studying the dynamics of collective spin structures [71]. The presence of kink/dip type anomaly in the magnetic field dependent AC-susceptibility (χ*'(H)*) curve has been extensively used as an indirect tool to probe the skyrmion phase in several skyrmion hosting materials [33, 72, 73, 74, 75, 76]. In contrast, the χ*'(H)* curve shows a smooth and continuous behaviour rather than any anomaly for the microscopic non-coplanar spin texture with non-zero spin chirality [41]. Therefore, we collected χ*'(H)* data of the Mn_2CoAl compound to explore the possible non-trivial spin texture, which gives rise to the THE.

4.2.2 AC-susceptibility Measurement

We performed χ*'(H)* measurement at various temperatures up to a field range of $\pm$1 T, as shown in Fig. 4.5. The χ*'(H)* curves do not exhibit any anomaly around the field where a large THE is found, as depicted in the inset of Fig. 4.5. This indicates that the THE observed in the bulk Mn_2CoAl compound is not associated with any skyrmion-type topological spin texture. In addition, the value of ρ_T in our studied compound is significantly larger than the values reported in most of the bulk systems exhibiting a skyrmionic phase [6, 20, 33, 35, 41]. The size of the topologically stable

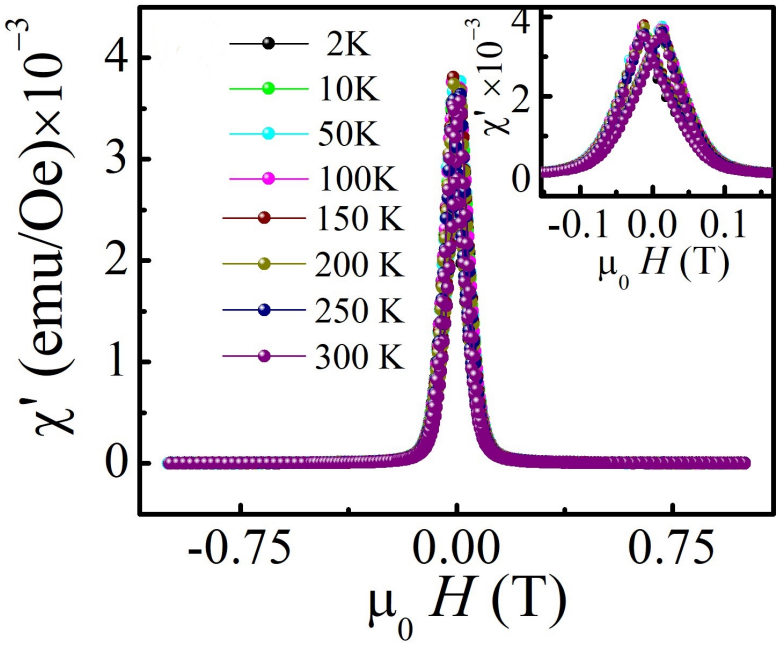

Figure 4.5: Magnetic field dependent AC-susceptibility ($\chi'(H)$) data at different temperatures. Inset shows the zoomed view of AC-susceptibility data in the lower magnetic field region.

skyrmion like mesoscopic non-coplanar spin texture [6] varies in the range 100–200 nm, giving rise to ρ_T in the order of nΩ-cm [34, 41]. Since, the value of ρ_T is inversely proportional to the size (density) of the non-coplanar spin texture, it is expected that the observed ρ_T in the Mn_2CoAl compound, which is in the order of $\mu\Omega$-cm, is resulted from the microscopic non-coplanar spin structure [41] with size of a few nanometers [6].

Now, to gain insight into the spin texture of the Mn_2CoAl compound, we looked at its crystal structure and the type of exchange interaction present among the magnetic atoms. The Mn_2CoAl compound exhibits a cubic crystal structure (space group $F\bar{4}3m$), as shown in Fig. 4.6 (a). The similar crystal systems (cubic) such as Mn_3Ir [77] and GdPtBi [78] exhibit antiferromagnetism with a triangular lattice arrangement of magnetic atoms along the diagonal [111] direction. If we look at the crystal structure of the Mn_2CoAl compound particularly in the [111] direction as shown in Fig. 4.6 (b), we can observe a triangular lattice of magnetic atoms (Mn and Co) [zoomed view is shown in Fig. 4.6 (c)]. Previous theoretical studies on the Mn_2CoAl compound suggest antiferromagnetic intra-sublattice (Mn-Mn and Co-Co) interactions, along with ferro- and antiferromagnetic type inter-sublattice interactions [involving interaction of Co with Mn at 4c (0.25,0.25,0.25) and 4a (0,0,0) sites, respectively] [50, 51]. The antiferromagnetic intra-sublattice interaction [50, 51]

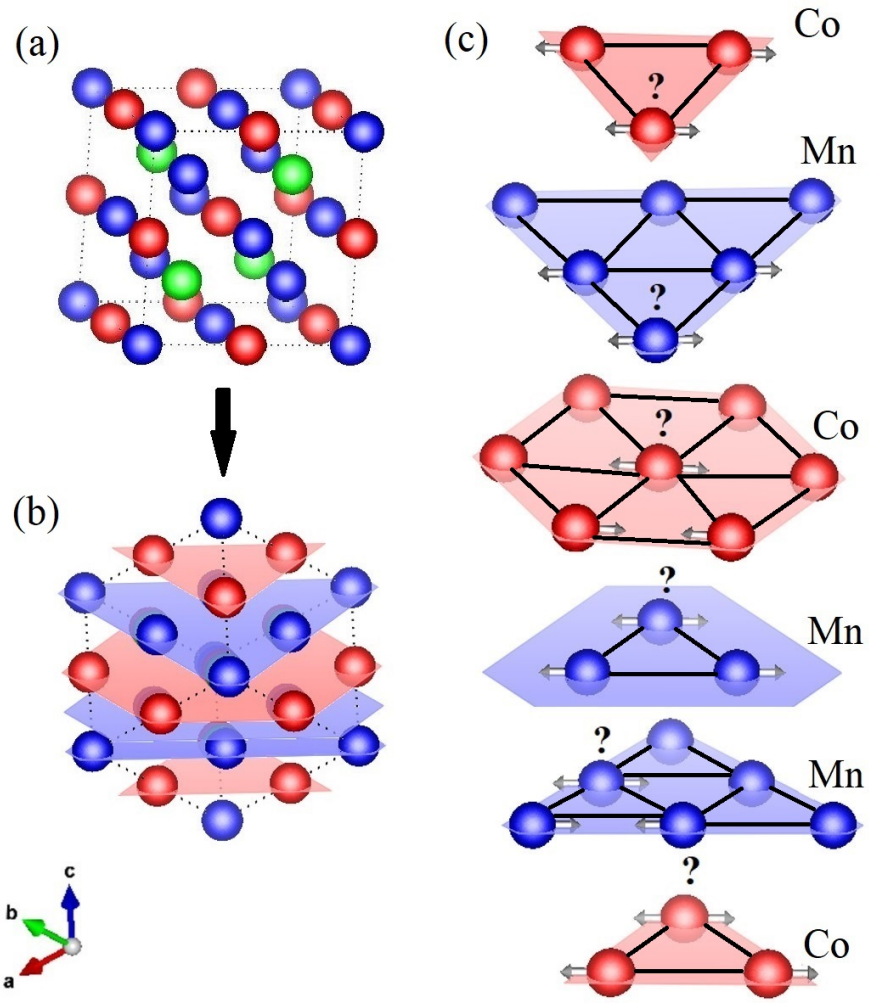

Figure 4.6: (a) XA type crystal structure of the Mn_2CoAl compound (blue, red and green spheres indicate the Mn, Co and Al atoms, respectively). (b) Rotated crystal structure along [111] direction. (c) Triangular lattice arrangement of magnetic atoms in [111] direction. Question mark represents the geometrically frustration on the triangular lattice.

may give rise to non-collinear spin texture due to geometrical frustration associated with the triangular lattice arrangement. In addition, the presence of both antiferromagnetic and ferromagnetic type inter-sublattice interaction [50, 51] along with the disorder [52] in the compound may develop strong magnetic frustration [49, 52]. It is well established that the MCA plays a crucial role in the formation of the non-coplanar spin texture [4, 27, 28, 31, 32]. Therefore, we calculated the MCA of the cubic Mn_2CoAl compound with the help of *M(H)* data using the law of approach to saturation method.

To calculate the MCA, we used the law of approach to saturation method, which involves the least-square fitting of *M(H)* data with the following expression [79]-

$$M = M_0(1 - \frac{A}{H^2}) + \chi.H \tag{4.3}$$

where, M_0, χ, and A are spontaneous magnetization, high field susceptibility, and constant, respectively. The fitting is shown in Fig. 4.7(a). With the help of the obtained value of parameter A, we calculated the value of the cubic MCA (K) by using the following relation [80]-

$$A = \frac{8}{105}(K^2/{M_0}^2) \tag{4.4}$$

We obtained the value of MCA (K) is $\sim$46 kJ/m^3 at 2 K, which is comparable to the value of K observed for the NiMnIn cubic system [42]. In the NiMnIn cubic Heusler compound, the THE has been reported due to the formation of non-coplanar spin texture in which cubic MCA plays a crucial role. Therefore, we argue that the MCA in the cubic Mn_2CoAl compound itself could lead to the emergence of non-coplanar spin texture. The inset of Fig. 4.7 (a) shows the variation of K value with temperature, which follows the similar behavior as ρ_T. It demonstrates that the MCA has a significant effect on the formation of non-coplanar spin texture [29]. Upon increasing the temperature, the declination in MCA gradually lowers the competition with different exchange energies, thus leading to the reduction in ρ_T [29, 31]. Therefore, our findings suggest that the MCA competing with the ferromagnetic and antiferromagnetic exchange interaction may give rise to the non-coplanar spin texture, which is responsible for the observed THE [29, 31].

To further confirm the formation of the non-coplanar spin texture, we have performed a micromagnetic simulation to theoretically simulate the magnetic structure by considering cubic MCA, exchange stiffness constant (A_{ex}) (linked with the exchange interaction among magnetic atoms). Before performing the micromagnetic simulation, we have calculated the A_{ex} by using *M(H)* data. The exchange stiffness coefficient (A_{ex}) represents the strength of direct exchange interactions among neighboring spins. The demagnetization of magnetic materials often induces the excitation of spin waves. The excitation energy can be estimated in terms of the spin-wave stiffness coefficient (D) [81]. At low temperatures, the amplitude of the spin wave will be small, and therefore the non-interacting spin wave may approximate the ground state excitation. To determine the A_{ex}, a theory

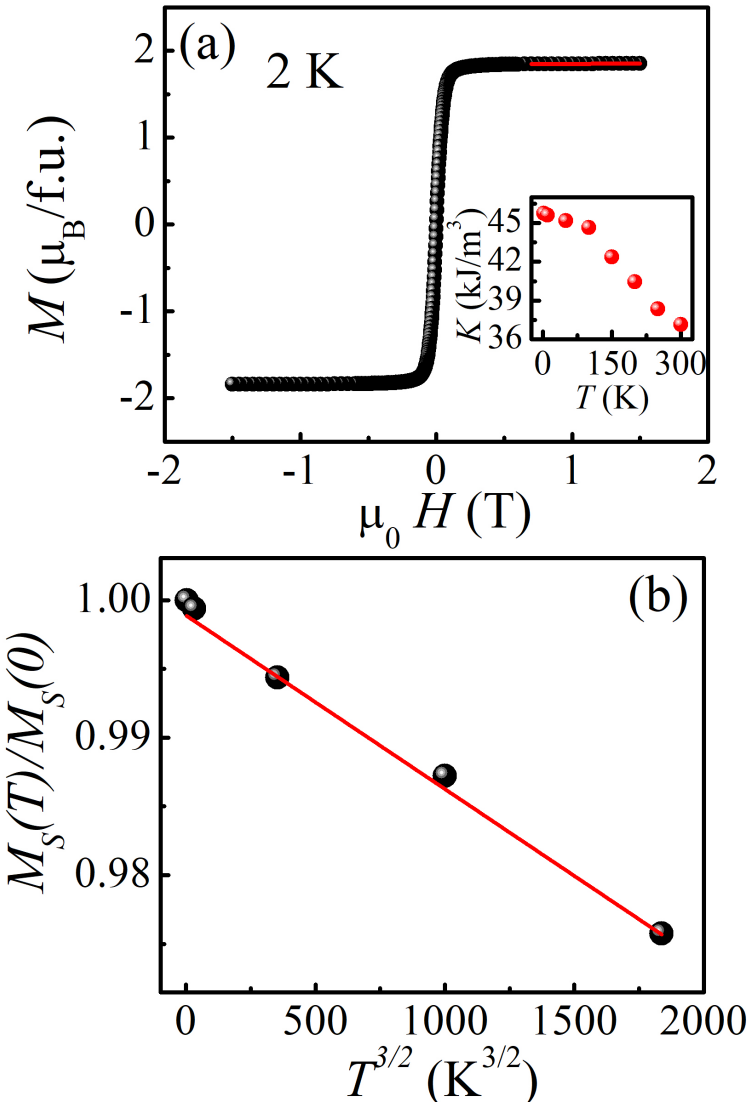

Figure 4.7: (a) Fitting of high field magnetization versus magnetic field data by using Eq.(4.1). Inset shows the variation of cubic MCA with temperature. (b) Fitting of temperature-dependence ($T^{3/2}$) of magnetization ratio ($M_S(T)/M_S(0)$) at low temperatures, measured at 1.5 T field for the Mn_2CoAl compound.

was proposed by Landau and Lifshitz [82]. In this method, one first finds the D by fitting the temperature dependence of spontaneous magnetization to Bloch's law, which describes the low-temperature magnetization [83, 84]-

$$\frac{M_S(T)}{M_S(0)} = 1 - BT^{3/2} \tag{4.5}$$

and,

$$B = 2.612\frac{g\mu_B}{M_S(0)}\left(\frac{k_B}{4\pi D}\right)^{3/2} \tag{4.6}$$

where $M_S(T)$, $M_S(0)$, μ_B, g, and k_B are spontaneous magnetization at temperature T, spontaneous magnetization at 0 K, Bohr magneton, Lande's splitting factor, and Boltzmann constant, respectively. The fitting shown in Fig. 4.7(b) gives the value of B and, thus, the value of D is calculated using Eq.(4.4). Further, the A_{ex} can be estimated by using the following relation [85]-

$$D = \frac{2A_{\mathrm{ex}} g \mu_{\mathrm{B}}}{M_S} \tag{4.7}$$

The value of A_{ex} at 2 K is calculated to be 4.8×10^{-12} J/m.

4.2.3 Micromagnetic Theory

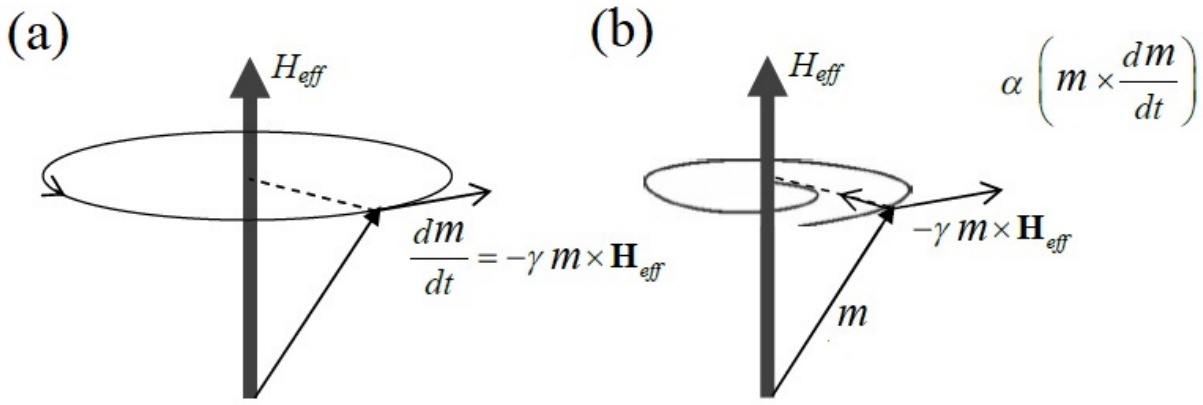

Figure 4.8: (a) Schematic representation of magnetization (m) precession around effective field (H_{eff}) without energy losses. (b) Precession of m around H_{eff} in the presence of energy losses leading to the damping of magnetization [86].

The theory of micromagnetics provides a solution to the time-dependent Landau–Lifshitz–Gilbert (LLG) equation, which offers insight into the dynamics of magnetization (m) influenced by an externally applied effective field (H_{eff}). The magnetization dynamics of a system at finite temperature is described by the LLG equation as follows [87, 88, 89]-

$$\frac{dm}{dt} = -|\gamma| m \times H_{eff} + \alpha\left(m \times \frac{dm}{dt}\right) \tag{4.8}$$

where the first term on the right-hand side of the LLG equation indicates that there is an angle between m and H_{eff} due to the torque experienced by the magnetization under the H_{eff}. The magnetization precesses around the direction of H_{eff} [Fig.4.8 (a)] as a consequence of the torque. The torque due to the H_{eff} is proportional to the time derivative/evolution of m and the constant of proportionality is called gyromagnetic ratio (γ). The second term on the right-hand side of the LLG equation describes the effect of dissipative phenomena and energy loss, which prevents the precession of magnetization indefinitely. The parameter α is a constant, called damping constant. Fig.4.8 (b) illustrates that the dissipative phenomena/energy loss leads to the damping of magnetization, which brings the magnetization in the direction of H_{eff}. The H_{eff} is expressed as [90, 91]-

$$H_{eff} = -\left(\frac{1}{\mu_0 M_S}\right)\left(\frac{dE_{total}}{dm}\right) \tag{4.9}$$

here μ_0 represents permeability in vacuum and E_{total} is the total magnetic energy of the system, which is given by Brown's equation [91, 92, 93]-

$$E_{total} = \int (E_{ex} + E_a + E_z + E_d + E_{DMI}) dV \tag{4.10}$$

The terms E_{ex}, Ea, E_z, E_d, and E_{DMI} represent exchange energy, anisotropy energy, Zeeman energy, demagnetization energy, and Dzyaloshinskii-Moriya interaction (DMI) energy, respectively. The micromagnetic simulations are carried out by repeatedly solving the LLG equation.

The Object-Oriented Micromagnetic Framework (OOMMF) utilizes the Finite Difference Method (FDM) to solve the Landau-Lifshitz-Gilbert (LLG) equation. This approach necessitates the division of the sample into identically-sized parallelepipeds called cells. The OOMMF Micromagnetic Input Format (MIF) contains essential input parameters and initial conditions for addressing any problem. Within each cell, physical properties like total energy (E_{total}) and magnetization (m) are computed based on the specified input energy parameters. The magnetization update process within each cell can be executed using two distinct evolvers: a time evolver, which tracks the dynamics of the LLG, and the energy minimization evolver, which locates local minima in the energy surface through direct minimization techniques. Evolvers are controlled by drivers and should be matched with the

suitable driver type, such as time evolvers with time drivers (Oxs_TimeDriver) and minimization evolvers (Oxs_MinDriver) with minimization drivers [94]. There are currently three time evolvers and one energy minimization evolver in the standard OOMMF distribution. The time evolvers are Oxs_EulerEvolve, Oxs_RungeKuttaEvolve, and Oxs_SpinXferEvolve [88]. The Oxs_EulerEvolve (Euler evolver) implements a simple first-order forward Euler method with step size control on the Landau-Lifshitz as an ordinary differential equation (ODE) in time. The Oxs_RungeK- uttaEvolve (4th-order Runge-Kutta evolver) uses several Runge-Kutta methods for integrating the Landau-Lifshitz-Gilbert ODE, with step size control. In most cases, it will greatly surpass the Oxs_ EulerEvolve class. The Oxs_SpinXferEvolve integrates an Landau-Lifshitz-Gilbert ODE augmented with a spin momentum term. The energy minimization evolver is Oxs_CGEvolve, which is an in-development conjugate gradient minimizer with no preconditioning [88]. The evolvers and corresponding drivers facilitate the transformation of the magnetic state from an initial configuration, obeying either Landau-Lifshitz-Gilbert (LLG) dynamics or direct energy minimization. Here, we have performed micromagnetic simulation using the energy minimization evolver (Oxs_CGEvolve).

4.2.4 Micromagnetic Simulation

A detailed micromagnetic simulation has been performed using Object Oriented MicroMagnetic Framework (OOMMF) software package [95]. The micromagnetic simulations are carried out on the area of 600×600×75 nm^3 with the cell size of 10×10×5 nm^3. The value of A_{ex}, K, and saturation magnetization used in the simulation are 4.8×10^{-12} J/m, 46 kJ/m^3, and 3.46×10^5 A/m , respectively, which are obtained from the experimental data. The studied compound stabilizes the non-coplanar spin texture at 0.1 T magnetic field [a clear view is shown in Fig 4.9 (a)], which is comparable with the field where the experimental maximum THE is observed. On increasing the magnetic field, the system is going towards field polarized state as shown at 0.2 T field in Fig 4.9 (b). For the magnetic fields $\geq$0.3 T, pure field polarized states are observed as shown in Fig 4.9 (c) and (d), and no change is observed on further increase in the magnetic field, which is consistent with the experimental observation that the THE vanishes above the field around 0.3 T. Similar behavior is observed for simulations with the negative applied magnetic field. Therefore, a detailed experimental and theoretical observations suggest that the THE observed in the Mn_2CoAl compound may arise due to the

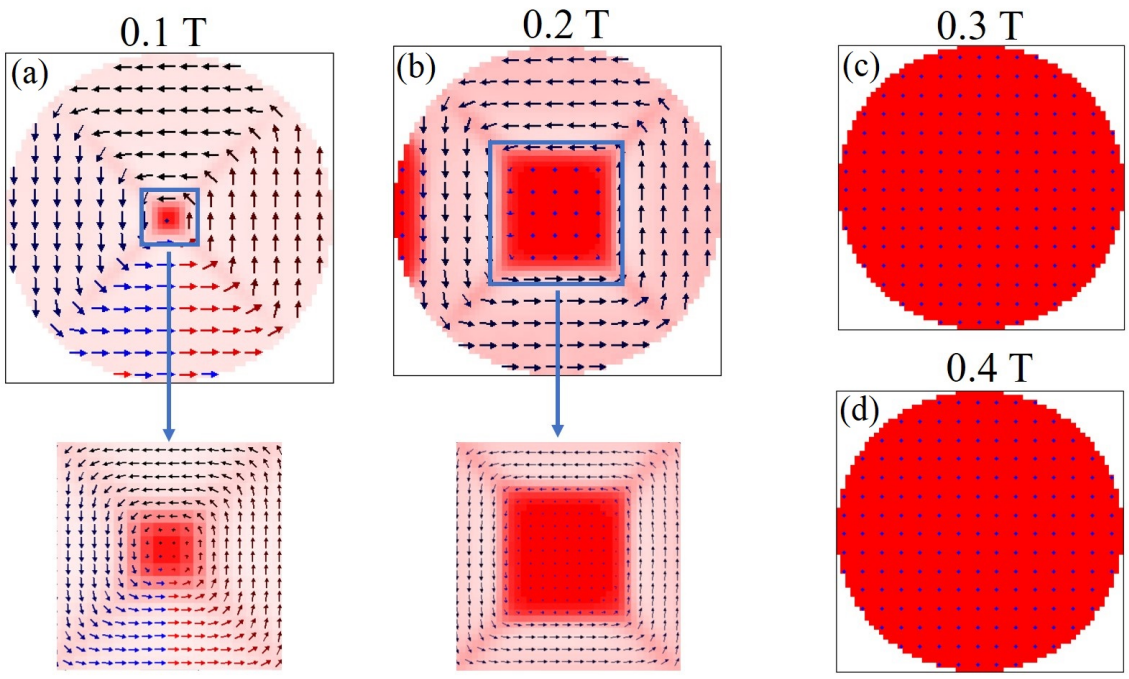

Figure 4.9: Simulated spin textures at different fields, (a) Non-coplanar spin texture at 0.1 T. (b) Nearly polarized spin texture at 0.2 T. (c) Fully polarized spin texture at 0.3 T. (d) Fully polarized spin texture at 0.4 T.

formation of non-coplanar spin texture as the result of the competition between the cubic MCA, and the ferro- and antiferromagnetic exchange interactions.

4.3 Conclusions

To conclude, we report a giant THE across a wide temperature range (2-300 K) by performing the magneto-transport measurements in the bulk Mn_2CoAl compound. The magnetic field-dependent AC-susceptibility measurements exhibit a smooth and continuous behaviour without any anomaly, suggests that the THE arises due to the microscopic non-coplanar magnetic texture. The existence of similar behaviour of the THE and the cubic MCA with temperature suggests that the interplay between the cubic MCA, the ferro- and antiferromagnetic exchange interactions may develop the non-coplanar spin texture, which is responsible for the THE observed in the bulk system of the Mn_2CoAl compound. This is further supported by the micromagnetic simulations, which reveal the presence of the possible non-coplanar spin structure. Our finding opens the possibility to search for the THE in previously unexplored cubic Heusler compounds, which can be a fruitful platform for

future spintronic applications.

References

[1] N. Nagaosa, Y. Tokura, Topological properties and dynamics of magnetic skyrmions. Nature Nanotech. **8**, 899–911 (2013).

[2] H. Takagi, R. Takagi, S. Minami, T. Nomoto, K. Ohishi, M.-T. Suzuki, Y. Yanagi, M. Hirayama, N. D. Khanh, K. Karube, H. Saito, D. Hashizume, R. Kiyanagi, Y. Tokura, R. Arita, T. Nakajima, and S. Seki, Spontaneous topological Hall effect induced by non-coplanar antiferromagnetic order in intercalated van der Waals materials. Nat. Phys. **19**, 961–968 (2023)

[3] M. Raju, A. P. Petrović, A. Yagil, K. S. Denisov, N. K. Duong, B. Göbel, E. Şaşıoğlu, O. M. Auslaender, I. Mertig, I. V. Rozhansky, and C. Panagopoulos, Colossal topological Hall effect at the transition between isolated and lattice-phase interfacial skyrmions. Nat. Commun. **12**, 2758 (2021).

[4] C. Sürgers, G. Fischer, P. Winkel, and H. v. Löhneysen, Large topological Hall effect in the non-collinear phase of an antiferromagnet. Nat. Commun. **5**, 3400 (2014).

[5] Y. Chen, Y. Zhu, R. Lin, W. Niu, R. Liu, W. Zhuang, X. Zhang, J. Liang, W. Sun, Z. Chen, Y. Hu, F. Song, J. Zhou, D. Wu, B. Ge, H. Yang, R. Zhang, X. Wang, Observation of Colossal Topological Hall Effect in Noncoplanar Ferromagnet Cr_5Te_6 Thin Films. Adv. Funct. Mater., 2302984 (2023).

[6] Y. He, S. Schneider, T. Helm, J. Gayles, D. Wolf, I. Soldatov, H. Borrmann, W. Schnelle, Rudolf Schaefer, G. H. Fecher, B. Rellinghaus and C. Felser, Topological Hall effect arising from the mesoscopic and microscopic non-coplanar magnetic structure in MnBi. Acta Materialia **226**, 117619 (2022).

[7] H. Wang, Y.g Dai, G.-M. Chow, and J. Chen, Topological hall transport: Materials, mechanisms and potential applications. Prog. Mater. Sci. **130**, 100971 (2022).

[8] P.-X. Qin, H. Yan, X.-N. Wang, Z.-X. Feng, Hui-Xin Guo, X.-R. Zhou, H.-J. Wu, X. Zhang, Z.-

G.-G. Leng, H.-Y. Chen, Z.-Q. Liu, Noncollinear spintronics and electric-field control: a review. Rare Met. **39**, 95–112 (2020).

[9] B. Göbel and I. Mertig, Quaternary-Digital Data Storage Based on Magnetic Bubbles in Anisotropic Materials. Phys. Rev. Applied **15**, 064052 (2021).

[10] B. Göbel and I. Mertig and O. A. Tretiakov, Beyond skyrmions: Review and perspectives of alternative magnetic quasiparticles. Phys. Rep. **895**, 1-28 (2021).

[11] P. Bruno, V. K. Dugaev, and M. Taillefumier, Topological Hall Effect and Berry Phase in Magnetic Nanostructures. Phys. Rev. Lett. **93**, 096806 (2004).

[12] T. Kurumaji, T. Nakajima, M. Hirschberger, A. Kikkawa, Y. Yamasaki, H. Sagayama, H. Nakao, Y. Taguchi, T.-h. Arima, Y. Tokura, Skyrmion lattice with a giant topological Hall effect in a frustrated triangular-lattice magnet. Science **365**,914-918 (2019).

[13] E. H. Hall, On a New Action of the Magnet on Electric Currents. Amer. J. Math. **2**, 287-292 (1879).

[14] N. Nagaosa, J. Sinova, S. Onoda, A. H. MacDonald, and N. P. Ong, Anomalous Hall effect. Rev. Mod. Phys. **82**, 1539 (2010).

[15] Z. Fang, N. Nagaosa, K. S. Takahashi, A. Asamitsu, R. Mathieu, T. Ogasawara, H. Yamada, M. Kawasaki, Y. Tokura, and K. Terakura, The Anomalous Hall Effect and Magnetic Monopoles in Momentum Space. Science **302**, 92-95 (2003).

[16] R. Karplus and J. M. Luttinger, Hall Effect in Ferromagnetics. Phys. Rev. **95**, 1145 (1954).

[17] J. Smit and J. Volger, The spontaneous Hall effect in ferromagnetics II. Physica (Amsterdam) **24**, 39-51 (1958).

[18] L. Berger, Side-Jump Mechanism for the Hall Effect of Ferromagnets. Phys. Rev. B **2**, 4559-4566 (1970).

[19] L. Vistoli, W. Wang, A. Sander, Q. Zhu, B. Casals, R. Cichelero, A. Barthélémy, S. Fusil, G. Heranz, S. Valencia, R. Abrudan, E. Weschke, K. Nakazawa, H. Kohno, J. Santamaria, W. Wu,

V. Garcia, M. Bibes, Giant Topological Hall Effect in Correlated Oxide Thin Films. Nat. Phys. **15**, 67−72 (2019).

[20] A. Neubauer, C. Pfleiderer, B. Binz, A. Rosch, R. Ritz, P. G. Niklowitz, and P. Böni, Topological Hall Effect in the A Phase of MnSi. Phys. Rev. Lett. **102**, 186602 (2009).

[21] N. Kanazawa, Y. Onose, T. Arima, D. Okuyama, K. Ohoyama, S. Wakimoto, K. Kakurai, S. Ishiwata, and Y. Tokura, Large Topological Hall Effect in a Short-Period Helimagnet MnGe. Phys. Rev. Lett. **106**, 156603 (2011).

[22] S. X. Huang and C. L. Chien, Extended Skyrmion Phase in Epitaxial FeGe (111) Thin Films. Phys. Rev. Lett. **108**, 267201 (2012).

[23] M. Nakamura, D. Morikawa, X. Yu, F. Kagawa, T. Arima, Y. Tokura, and M. Kawasaki, Emergence of Topological Hall Effect in Half-Metallic Manganite Thin Films by Tuning Perpendicular Magnetic Anisotropy. J. Phys. Soc. Jpn. **87**, 074704 (2018).

[24] K. G. Rana, O. Meshcheriakova, J. Kübler, B. Ernst, J. Karel, R. Hillebrand, E. Pippel, P. Werner, A. K. Nayak, C. Felser, and S. S. P. Parkin, Observation of topological Hall effect in Mn_2RhSn films. New J. Phys. **18**, 085007 (2016).

[25] Y. Li, B. Ding, X. Wang, H. Zhang, W. Wang, and Z. Liu, Large topological hall effect observed in tetragonal Mn_2PtSn Heusler thin film. Appl. Phys. Lett. **113**, 062406 (2018).

[26] G. Kimbell, C. Kim, W. Wu, M. Cuoco, and J. W. A. Robinson, Challenges in identifying chiral spin textures via the topological Hall effect. Commun. Mater. **3**, 19 (2022).

[27] Z. H. Liu, Y. J. Zhang, G. D. Liu, B. Ding, E. K. Liu, H. M. Jafri, Z. P. Hou, W. H. Wang, X. Q. Ma, and G. H. Wu, Transition from Anomalous Hall Effect to Topological Hall Effect in Hexagonal Non-Collinear Magnet Mn_3Ga. Sci Rep **7**, 515 (2017).

[28] Y. Shiomi, M. Mochizuki, Y. Kaneko, and Y. Tokura, Hall Effect of Spin-Chirality Origin in a Triangular-Lattice Helimagnet $Fe_{1.3}Sb$. Phys. Rev. Lett. **108**, 056601 (2012).

[29] J. Liu, S. Zuo, X. Zheng, Y. Zhang, T. Zhao, F. Hu, J. Sun, B. Shen, Magnetic transition

behavior and large topological Hall effect in hexagonal $Mn_{2-x}Fe_{1+x}Sn$ (x=0.1) magnet. Appl. Phys. Lett. **117**, 052407 (2020).

[30] J. Liu, S.L. Zuo, J. Shen, Y. Zhang, Y. Zhang, Z.X. Li, X.Q. Gao, H.F. Kang, T.Y. Zhao, F.X. Hu, J. Sun and B.G. Shen, Large topological Hall effect and in situ observation of magnetic domain structures in the Mn_2FeSn compound. Mater. Today Phys. **29**, 100871 (2022).

[31] V. Kumar, G. K. Shukla, N. Shahi, S. Singh, Topological Hall Effect in $(Mn_{1-x}Fe_x)_{3.25}Ge$ (x = 0.4) Hexagonal Magnet. Phys. Status Solidi RRL 2300174 (2023).

[32] N. J. Ghimire, R. L. Dally, L. Poudel, D. C. Jones, D. Michel, N. T. Magar, M. Bleuel, M. A. McGuire, J. S. Jiang, J. F. Mitchell, J. W. Lynn and I. I. Mazin, Competing magnetic phases and fluctuation-driven scalar spin chirality in the kagome metal YMn_6Sn_6. Sci. Adv. **6**, eabe2680 (2020).

[33] S. Sen, C. Singh, P. K. Mukharjee, R. Nath, and A. K. Nayak, Observation of the topological Hall effect and signature of room-temperature antiskyrmions in Mn-Ni-Ga D_{2d} Heusler magnets. Phys. Rev. B **99**, 134404 (2019).

[34] A. K. Nayak, V. Kumar, T. Ma, P. Werner, E. Pippel, R. Sahoo, F. Damay, U. K. Rößler, C. Felser, and S. S. P. Parkin, Magnetic antiskyrmions above room temperature in tetragonal Heusler materials. Nature **548**, 561 (2017).

[35] V. Kumar, N. Kumar, M. Reehuis, J. Gayles, A. S. Sukhanov, A. Hoser, F. Damay, C. Shekhar, P. Adler, and C. Felser, Detection of antiskyrmions by topological Hall effect in Heusler compounds. Phys. Rev. B **101**, 014424 (2020).

[36] W. Wang, Y. Zhang, G. Xu, L. Peng, B. Ding, Y. Wang, Z. Hou, X. Zhang, X. Li, E. Liu, S. Wang, J. Cai, F. Wang, J. Li, F. Hu, G. Wu, B. Shen, and X.-X. Zhang, A Centrosymmetric Hexagonal Magnet with Superstable Biskyrmion Magnetic Nanodomains in a Wide Temperature Range of 100–340 K. Adv. Mater. **28**, 6887–6893 (2016).

[37] K. Manna, Y. Sun, L. Muechler, J. Kübler, and C. Felser, Heusler, Weyl and Berry. Nat. Rev. Mater. **3**, 244 (2018).

[38] L. Wollmann, A. K. Nayak, S. S. P. Parkin, and C. Felser, Heusler 4.0: Tunable Materials. Annu. Rev. Mater. Res. **47**, 247 (2017).

[39] P. Vir, J. Gayles, A. S. Sukhanov, N. Kumar, F. Damay, Y. Sun, J. K¨ubler, C. Shekhar, and C. Felser, Anisotropic topological Hall effect with real and momentum space Berry curvature in the antiskrymion-hosting Heusler compound $Mn_{1.4}PtSn$. Phys. Rev. B **99**, 140406 (2019).

[40] X. Xiao, L. Peng, X. Zhao, Y. Zhang, Y. Dai, J. Guo, M. Tong, J. Li, B. Li, W. Liu, J. Cai, B. Shen, and Z. Zhang, Low-field formation of room-temperature biskyrmions in centrosymmetric MnPdGa magnet. Appl. Phys. Lett. **114**, 142404 (2019).

[41] B. Giri, A. I. Mallick, C. Singh, P. V. P. Madduri, F. Damay, A. Alam, and A. K. Nayak, Robust topological Hall effect driven by tunable noncoplanar magnetic state in Mn-Pt-In inverse tetragonal Heusler alloys. Phys. Rev. B **102**, 014449 (2020).

[42] W. Zhang, B. Balasubramanian, A. Ullah, R. Pahari, X. Li, L. Yue, S. R. Valloppilly, A. Sokolov, R. Skomski, and D. J. Sellmyer, Comparative study of topological Hall effect and skyrmions in NiMnIn and NiMnGa. Appl. Phys. Lett. **115**, 172404 (2019).

[43] A. Kundu, S. Ghosh, R. Banerjee, S. Ghosh, and B. Sanyal, New quaternary half-metallic ferromagnets with large Curie temperatures. Sci Rep **7**, 1803 (2017)

[44] S. Ouardi, G. Fecher, C. Felser, and J. Kübler, Realization of Spin Gapless Semiconductors: The Heusler Compound Mn_2CoAl. Phys. Rev. Lett. **110**, 100401 (2013).

[45] Z. Yue, Z. Li, L. Sang, and X. Wang, Spin-Gapless Semiconductors. Small **16** 1905155 (2020).

[46] X. L. Wang, Proposal for a New Class of Materials: Spin Gapless Semiconductors. Phys. Rev. Lett., **100**, 156404 (2008).

[47] B. M. Ludbrook, G. Dubuis, A.-H. Puichaud, B. J. Ruck, and S. Granvill, Nucleation and annihilation of skyrmions in Mn_2CoAl observed through the topological Hall effect. Sci Rep **7**, 13620 (2017).

[48] A. Ullah, B. Balamurugan, W. Zhang, S. Valloppilly, X.-Z. Li, R. Pahari, L.-P. Yue, A. Sokolov,

D. J. Sellmyer, and R. Skomski, Crystal Structure and Dzyaloshinski–Moriya Micromagnetics. IEEE Trans. Magn. **55**, 7100305 (2019).

[49] M. E. Jamer, B. A. Assaf, T. Devakul, and D. Heiman, Magnetic and transport properties of Mn_2CoAl oriented films. Appl. Phys. Lett. **103**, 142403 (2013).

[50] M. Meinert, J.-M. Schmalhorst, and G. Reiss, Exchange interactions and Curie temperatures of Mn_2CoZ compounds. J. Phys.: Condens. Matter **23**, 116005 (2011).

[51] A. Jakobsson, P. Mavropoulos, E. Şaşıoğlu, S. Blügel, M. Ležaić, B. Sanyal, and I. Galanakis, First-principles calculations of exchange interactions, spin waves, and temperature dependence of magnetization in inverse-Heusler-based spin gapless semiconductors. Phys. Rev. B **91**, 174439 (2015).

[52] N. Shahi, A. K. Jena, G. K. Shukla, V. Kumar, S. Rastogi, K. K. Dubey, I. Rajput, S. Baral, A. Lakhani, S.-C. Lee, S. Bhattacharjee, and S. Singh, Antisite disorder and Berry curvature driven anomalous Hall effect in the spin gapless semiconducting Mn_2CoAl Heusler compound. Phys. Rev. B **106**, 245137 (2022).

[53] J. Yi, H. Zhuang, Q. Zou, Z. Wu, G. Cao, S. Tang, S. A. Calder, P. R. C. Kent, D. Mandrus, Z. Gai, Competing antiferromagnetism in a quasi-2D itinerant ferromagnet: Fe_3GeTe_2. 2D Materials **4** 011005 (2016).

[54] Y. You, Y. Gong, H. Li, Z. Li, M. Zhu, J. Tang, E. Liu, Y. Yao, G. Xu, F. Xu, and W. Wang, Angular dependence of the topological Hall effect in the uniaxial van der Waals ferromagnet Fe_3GeTe_2. Phys. Rev. B **100**, 134441 (2019).

[55] H. Li, K. Hayashi, Y. Nagashima, S. Yoshioka, J. Dong, J.-F. Li, and Y. Miyazaki, Effects of Disorder on the Electronic Structure and Thermoelectric Properties of an Inverse Full-Heusler Mn_2CoAl Alloy. Chem. Mater. **33**, 2543-2547 (2021).

[56] P. Swekis, A. Markou, D. Kriegner, J. Gayles, R. Schlitz, W. Schnelle, S. T. B. Goennenwein, and Claudia Felser. Topological Hall effect in thin films of $Mn_{1.5}PtSn$. Phys. Rev. Mater. **3**, 013001(R) (2019).

[57] G. K. Shukla, A. K. Jena, N. Shahi, K. K. Dubey, I. Rajput, S. Baral, K. Yadav, K. Mukherjee,

A. Lakhani, K. Carva, S.-C. Lee, S. Bhattacharjee, and S. Singh, Atomic disorder and Berry phase driven anomalous Hall effect in a Co_2FeAl Heusler compound. Phys. Rev. B **105**, 035124 (2022).

[58] G. K. Shukla, J. Sau, N. Shahi, A. K. Singh, M. Kumar, and S. Singh, Anomalous Hall effect from gapped nodal line in the Co_2FeGe Heusler compound. Phys. Rev. B **104**, 195108 (2021).

[59] S. Roychowdhury, S. Singh, S. Guin, N. N. Kumar, T. Chakraborty, W. Schnelle, H. Borrmann, C. Shekhar, C. Felser, Giant Topological Hall Effect in the Noncollinear Phase of Two-Dimensional Antiferromagnetic Topological Insulator $MnBi_4Te_7$. Chem. Mater. **33** 8343-8350 (2021).

[60] Q. Wang, Q. Yin, and H. Lei, Giant topological Hall effect of ferromagnetic kagome metal Fe_3Sn_2. Chin. Phys. B **29** 017101 (2020).

[61] X. Zheng, X. Zhao, J. Qi, X. Luo, S. Ma, C. Chen, H. Zeng, G. Yu, N. Fang, S. U. Rehman, W. Ren, B. Li, Z. Zhong, Giant topological Hall effect around room temperature in noncollinear ferromagnet $NdMn_2Ge_2$ single crystal. Appl. Phys. Lett. **118** 072402 (2021).

[62] C. Zhang, C. Liu, J. Zhang, Y. Yuan, Y. Wen, Y. Li, D. Zheng, Q. Zhang, Z. Hou, G. Yin, K. Liu, Y. Peng, and X.-X. Zhang, Room-Temperature Magnetic Skyrmions and Large Topological Hall Effect in Chromium Telluride Engineered by Self-Intercalation, Adv. Mater. **35** 2205967 (2023).

[63] Z. H. Liu, A. Burigu, Y.J. Zhang, H. M. Jafri, X.Q. Ma, E.K. Liu, W.H. Wang, and G.H. Wu, Giant topological Hall effect in tetragonal Heusler alloy Mn_2PtSn, Scr. Mater. **143**, 122-125 (2018).

[64] X. Yao , J. Gaudet, R. Verma, D. E. Graf, H.-Y. Yang, F. Bahrami, R. Zhang, A. A. Aczel, S. Subedi , D. H. Torchinsky, J. Sun, A. Bansil, S.-M. Huang, B. Singh, P. Blaha , P. Nikolić, and F. Tafti, Large Topological Hall Effect and Spiral Magnetic Order in the Weyl Semimetal SmAlSi, Phys. Rev. X **13**, 011035 (2023).

[65] P. K. Rout, P. V. P. Madduri, S. K. Manna, and A. K. Nayak, Field-induced topological Hall effect in the noncoplanar triangular antiferromagnetic geometry of Mn_3Sn. Phys. Rev. B **99**, 094430 (2019).

[66] M. R. U. Nabi, A. Wegner, F. Wang, Y. Zhu, Y. Guan, A. Fereidouni, K. Pandey, R. Basnet, G. Acharya, H. O. H. Churchill, Z. Mao, and J. Hu, Giant topological Hall effect in centrosymmetric tetragonal $Mn_{2-x}Zn_xSb$. Phys. Rev. B **104**, 174419 (2021).

[67] G. Xu, D. Liu, L. He, S. Wang, L. Ma, A giant topological Hall effect in ferromagnetic compound $CeMn_2Ge_2$ with wide temperature range from 70 to 310 k. Mater. Lett. **315**, 131963 (2022).

[68] D. A. Mayoh, J. Bouaziz, A. E. Hall, J. B. Staunton, M. R. Lees, and G. Balakrishnan, Giant topological and planar Hall effect in $Cr_{1/3}NbS_2$. Phys. Rev. Res. **4**, 013134 (2022).

[69] Y. He, J. Kroder, J. Gayles, C. Fu, Y. Pan, W. Schnelle, C. Felser, and G. H. Fecher, Large topological Hall effect in an easy-cone ferromagnet $(Cr_{0.9}B_{0.1})Te$. Appl. Phys. Lett. **117**, 052409 (2020).

[70] H. Li, B. Ding, J. Chen, Z. Li, E. Liu, X. Xi, G. Wu, and W. Wang, Large anisotropic topological Hall effect in a hexagonal non-collinear magnet Fe_5Sn_3. Appl. Phys. Lett. **116**, 182405 (2020).

[71] M. Maus, AC Susceptometry for Characterizing Magnetic Spin Structures, Ph.D. thesis, University of Colorado, Boulder (2019).

[72] Sk Jamaluddin, S. K. Manna, B. Giri, P. V. P. Madduri, S. S. P. Parkin, and A. K. Nayak, Robust Antiskyrmion Phase in Bulk Tetragonal Mn–Pt(Pd)–Sn Heusler System Probed by Magnetic Entropy Change and AC-Susceptibility Measurements. Adv. Funct. Mater. **29**, 1901776 (2019).

[73] A. Bauer and C. Pfleiderer, Magnetic phase diagram of MnSi inferred from magnetization and ac susceptibility. Phys. Rev. B **85**, 214418 (2012).

[74] H. Wilhelm, M. Baenitz, M. Schmidt, U. K. Rößler, A. A. Leonov, and A. N. Bogdanov, Precursor Phenomena at the Magnetic Ordering of the Cubic Helimagnet FeGe. Phys. Rev. Lett. **107**, 127203 (2011).

[75] S. Seki, X. Z. Yu, S. Ishiwata, Y. Tokura, Observation of Skyrmions in a Multiferroic Material. Science **336** 198-201 (2012).

[76] P. V. Prakash Madduri, S. Sen, B. Giri, D. Chakrabartty, S. K. Manna, S. S. P. Parkin, and A.

K. Nayak, ac susceptibility study of magnetic relaxation phenomena in the antiskyrmion-hosting tetragonal Mn-Pt(Pd)-Sn system. Phys. Rev. B **102** 174402 (2020).

[77] H. Chen, Q. Niu, and A. H. MacDonald, Anomalous Hall Effect Arising from Noncollinear Antiferromagnetism. Phys. Rev. Lett. **112**, 017205 (2014).

[78] T. Suzuki, R. Chisnell, A. Devarakonda, Y.-T. Liu, W. Feng, D. Xiao, J. W. Lynn and J. G. Checkelsky, Large anomalous Hall effect in a half-Heusler antiferromagnet. Nature Phys. **12**, 1119–1123 (2016).

[79] G. Hadjipanayis, D. J. Sellmyer, B. Brandt, Rare-earth-rich metallic glasses. I. Magnetic hysteresis, Phys. Rev. B **23**, 3349 (1981).

[80] K. S. Sivaranjani, G. A. Jacob, and R. J. Joseyphus, Comprehensive Law-of-Approach-to-Saturation for the Determination of Magnetic Anisotropy in Soft Magnetic Materials. Phys. Status Solidi B **259**, 2200050 (2022).

[81] K. Mandal, S. Mitra, P. A. Kumar, Deviation from Bloch $T^{3/2}$ law in ferrite nanoparticles, Europhys. Lett. **75**, 618 (2006).

[82] E. Lifshitz, J. Phys. USSR **8**, 337 (1944).

[83] A. Franco, Jr. , H. V. Pessoni , F. L. Machado, Spin-wave stiffness parameter in ferrimagnetic systems: Nanoparticulate powders of (Mg,Zn)Fe_2O_4 mixed ferrites, J. Appl. Phys. **118**, 173904 (2015).

[84] R. Y. Umetsu, T. Kanomata, Spin stiffness constant of half-metallic ferrimagnet in Mn-based Heusler alloys, Phys. Procedia. **75**, 890 (2015).

[85] O. Šipr, S. Mankovsky, H. Ebert, Spin wave stiffness and exchange stiffness of doped permalloy via ab initio calculations, Phys. Rev. B **100**, 024435 (2019).

[86] L. Rohman, E. Purwandari, I. Romadhony, and D. Djuhana, Magnetic Properties of FePt Material Influenced by Heat-Assisted Using Micromagnetic Simulation, J. Phys.: Conf. Ser. **1491** 012013 (2020).

[87] T. Gilbert, A phenomenological theory of damping in ferromagnetic materials, IEEE Trans. Magn. **40**, 3443- 9 (2004).

[88] M. J. Donahue, D. G. Porter, OOMMF User's Guide, Version 1.0, Integracy Report NISTIR 6376, National Institute of Standards and Technology, Gaithersburg, MD, (Sept 1999).

[89] X. Zhang, J. Xia, Y. Zhou, X. Liu, H. Zhang, M. Ezawa, Skyrmion dynamics in a frustrated ferromagnetic film and current-induced helicity locking-unlocking transition, Nat. Commun. **8**, 1717 (2017).

[90] X. Zhang, G. P. Zhao, H. Fangohr, J. P. Liu, W. X. Xia, J. Xia, F. J. Morvan, Skyrmion-skyrmion and skyrmion-edge repulsions in skyrmion-based racetrack memory, Sci. Rep. **5**, 7643 (2015).

[91] J. E. Miltat, M. J. Donahue, Numerical micromagnetics: Finite difference methods, Handb Magn. Mater. **2**, 742-64 (2007).

[92] W. F. Brown, Micromagnetics, Interscience Publisher, NewYork, London (1963).

[93] R. Li, S. Zhang, S. Luo, Z. Guo, Y. Xu, J. Ouyang, M. Song, Q. Zou, L. Xi, X. Yang, J. Hong, A spin–orbit torque device for sensing three-dimensional magnetic fields, Nat. Electron. **4**, 179-84 (2021).

[94] S. S. Mahalingam, B. V. Manikandan, S. Arockiaraj, Review–micromagnetic simulation using OOMMF and experimental investigations on nano composite magnets, J. Phys. Conf. Ser **1172**, 012070 (2019)

[95] M. J. Donahue, D. G. Porter, OOMMF User's Guide, Version 1.0, Integracy Report NISTIR 6376, National Institute of Standards and Technology, Gaithersburg, MD, (Sept 1999).